



Project Title: Transforming Brain Surgery by Advancing Functional-Guided Neuronavigational Imaging

Project Acronym: HyperProbe

Grant Agreement: 101071040

Call Identifier: HORIZON-EIC-2021-PATHFINDERCHALLENGES-01

D5.1 Image processing pipelines for registration of pre- and intraoperative imaging

Leader Partner: UCBL

Work Package: WP5

Author(s): Charly Caredda, Eric Van-Reeth, Fernand Fort, Michaël Sdika, Bruno Montcel

Due date: Month 24

Actual delivery date: 30.09.2024

Type: OTHER

Dissemination level: PU

Contents

1	Introduction	3
2	Automatic registration pipeline	4
2.1	Projection of the T1 volume	6
2.2	Segmentation of the blood vessels MR and optical images	6
2.3	Registration procedure	7
2.4	Reconstruction of the optical image on the MRI volume	9
2.5	Projection of the MRI volume on the optical window	11
3	Validation of the registration algorithm	13
4	Areas for improvement	14

Abbreviations

- **MRI:** Magnetic Resonance Imaging
- **MR:** Magnetic Resonance
- **fMRI:** functional Magnetic Resonance Imaging
- **EBS:** Electrical brain stimulation
- **FLAIR:** Fluid attenuation inversion recovery
- **BOLD:** Blood Oxygen Level Dependent

Disclaimer

This project has received funding from the European Union’s Horizon 2020 research and innovation programme under grant agreement No. 952172.

1 Introduction

The deliverable presents the image processing pipelines for the registration of pre- and postoperative MRI acquisitions of the patient's brain with intraoperative optical images of the patient's exposed brain cortex. This pipeline automatically co-localizes intraoperative optical and preoperative MRI measurements, is totally included in the clinical practice and does not need any specific medical device to be added in the operative room. Indeed, it only requires MRI volumes that are systematically acquired by the radiologists for brain tumor resection operations. This pipeline is proposed in the context of HyperProbe aims, which rely on the patient clinical pipeline represented in Fig. 1.

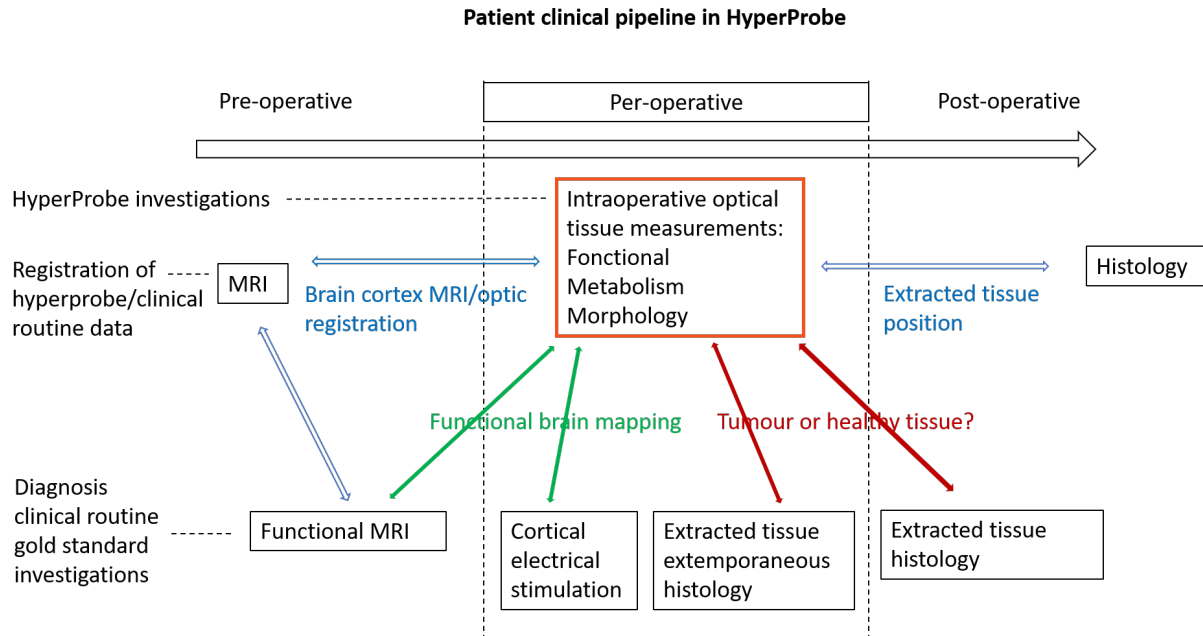


Figure 1: Clinical pipeline for patient undergoing a brain tumor resection operation. In the context of the Hyperprobe, specific intraoperative optical measurements (surrounded in orange) were added to the clinical practice. Intraoperative optical biomarkers and clinical gold standard biomarkers are linked by specific quantification models developed in WP5. Functional brain mapping biomarkers links are indicated by green arrows. Tumour/healthy status links are represented by red arrows. Blue arrows indicate the co-localization (spatial registration) of intraoperative optical and gold standard clinical measurements.

Pre-operative MRI acquisitions aim to assess the diagnosis of cancer and initiate the brain tumor surgery. Anatomical MRI acquisitions such as T1 and FLAIR volumes are used to identify the tumor in the patient brain and fMRI acquisitions allow the identification of brain functions. Using these identifications, the radiologist can define the intervention risk by calculating the distance between the brain function and the lesion.

During neurosurgery, the patient has undergone craniotomy to allow access to the cerebral cortex. The craniotomy induces a brain shift that invalidates the relevance of neuronavigation to localize functional areas during surgery [10]. To avoid localization errors, intraoperative MRI has been suggested [8], but it complicates the surgical procedure and is, therefore, rarely used. During neurosurgery, electrical brain stimulation (EBS) is the gold standard, but this technique is mainly limited by its low spatial resolution (≈ 5 mm [17]) and has the potential risk to trigger epileptic seizures. This technique allows a robust and reliable detection of many functional areas, but could be traumatic for the patient, by inhibiting certain cognitive functions such as speech for example. EBS is also complicated to perform and requires a very strong expertise. During the resection of the tumor, extracted tissues are controlled by histopathological measurements that could be guided by fluorescence imaging [9, 18].

In order to complement actual gold standards, the Hyperprobe devices 2 and 2.1 have the objective to assess functional, metabolic and morphological information of the brain tissue using hyperspectral imaging. To validate the tissue measurements, a comparison with pre- and intraoperative gold standards is required. The comparison with intraoperative histological and electrical brain stimulation measurements is direct since the localization of the controlled tissue is visible by imaging. However, the comparison with preoperative MRI acquisitions need the development of col-localization techniques. The objective is to only co-localize the brain cortex of MRI and optical acquisitions. Indeed, as shown on Fig. 1, fMRI is used as a brain mapping clinical gold standard to complement EBS. Hyperprobe devices will only

investigate a brain mapping before tumor resection with an intact brain cortex. Thus, there is no need for 3D co-localization between MRI and images acquired from hyperprobe devices, as the tumoral status gold standard is not MRI. During the resection, EBS and histological measurements will remain the gold standard techniques.

In the literature and in commercial systems, the comparison between optical measurements and preoperative MRI is conducted using a registration procedure based on landmarks [3, 4, 16]. These “landmarks” denote identical locations in optical images and MRI volumes and are obtained with clinical neuronavigation systems. This registration approach has two main disadvantages:

1. It requires the intervention of the neurosurgeon with the use of a neuro-navigation tool and thus increases the duration of the surgery.
2. Locations indicated by neuro-navigation tools are not totally accurate. For some patients, we observed 2 cm shifts between points identified by the neuro-navigation tool and those validated by the neurosurgeon.

Recently, Villa et al. [22] proposed a novel technique to register hyperspectral images on MRI. The technique is based on the use of a multimodal system during neurosurgery. The system is composed of a RGB-Depth and hyperspectral cameras. The RGB-Depth camera captures the patient’s facial geometry, which is used for registration with the preoperative MRI. Once MR depth registration is complete, the integration of HS data is achieved using a calibrated homography transformation. The hyperspectral camera is then moved to capture the craniotomy site. This technique aims to register optical images on MRI with a great precision (1.88 ± 0.19 mm) compared to the landmark-based technique (4.07 ± 1.28 mm). However, this technique has the major disadvantage of adding a dedicated device in the operating room, which changes the clinical routine. Moreover, moving the optical system during the calibration phase can be very complex. Operating room space is limited and moving the optical system can compromise the sterile area.

To overcome the limitations of current techniques, we propose to develop an automatic procedure that takes advantages of the common cerebral structures on the optical images and the anatomic MRI volumes: the large blood vessels, see Fig. 2.

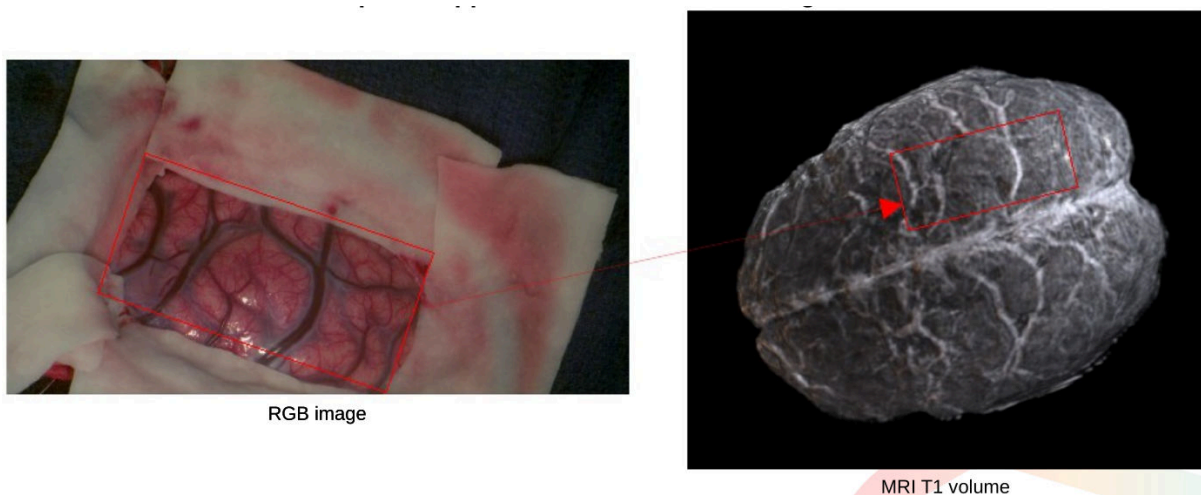


Figure 2: Intraoperative optical image and pre-operative MRI volume (T1 sequence with injection of Gadolinium) of patient 1.

In this report, we will describe the main blocks and parameters of the automatic registration pipeline and evaluate its performance with 9 patients. The code of this registration pipeline is available in a GitHub repository and the dataset of results can be found here.

2 Automatic registration pipeline

We represented the flowchart of the automatic registration pipeline in Fig. 3. This pipeline aims to register pre- and postoperative MRI acquisitions of the human brain with intraoperative optical images of the human brain cortex. The pipeline has been developed with Python with open-source frameworks, like

itk v5.4 [13, 24], itk-elastic v0.19.1 [15, 19], opencv v4.9 [2], scipy v1.12 [23] and scikit-image v0.22 [21]. These following images have to be acquired to process the registration procedure, see table 1.

Required data	International clinical standard	Standard at HCL - CHU Saint-Etienne	Field of view	Resolution
Preoperative T1 volume with injection of Gadolinium	✓	✓	Full head ($\approx 1\text{mm}^2$)	Clinical standard
Preoperative FLAIR volume	✓	✓	Full head ($\approx 1\text{mm}^2$)	Clinical standard
Tumor volume segmentation		✓	Full head ($\approx 1\text{mm}^2$)	Clinical standard
Intraoperative optical images			Entire surgical window The image is centered on the surgical window which is centered on the tumor	At least equivalent to that of the T1 volume ($\leq 1\text{mm}^2$)

Table 1: Imaging technique required to performed the automatic registration pipeline.

The use of the T1 and FLAIR MRI volumes does not change the clinical practice of the radiologists since these volumes are systematically acquired for each patient. T1 volume is usually named “neuronavigation volume”. This volume is used as reference: the other MRI volumes (FLAIR, tumor volume segmentation, fMRI) are registered on this volume. At Lyon and Saint-Etienne hospitals (HCL and CHU Saint-Etienne), the tumor volume is segmented from the T1 or FLAIR acquisitions by radiologists. This not systematically the case for other hospitals, but solutions can be implemented as proposed in section 4.

In the registration pipeline, the T1 and the tumor segmentation volumes were used to define a 2D projection of the T1 volume centered on the center of mass of the patient’s tumor (see section 2.1). The tumor is represented with a blue contour.

The blood vessels were enhanced in the MRI projection and in the optical image with a Hessian-based Frangi vesselness filter [7]. Then, the blood vessels were segmented with a thresholding procedure and the topology of the blood vessels was extracted with a skeletonization algorithm (see section 2.2).

Using the skeletons of the blood vessels in the MR and optical images, the similarity transform that best match the two images was calculated (see section 2.3). The registration procedure was initialized with 9 points located around the tumor to help the convergence.

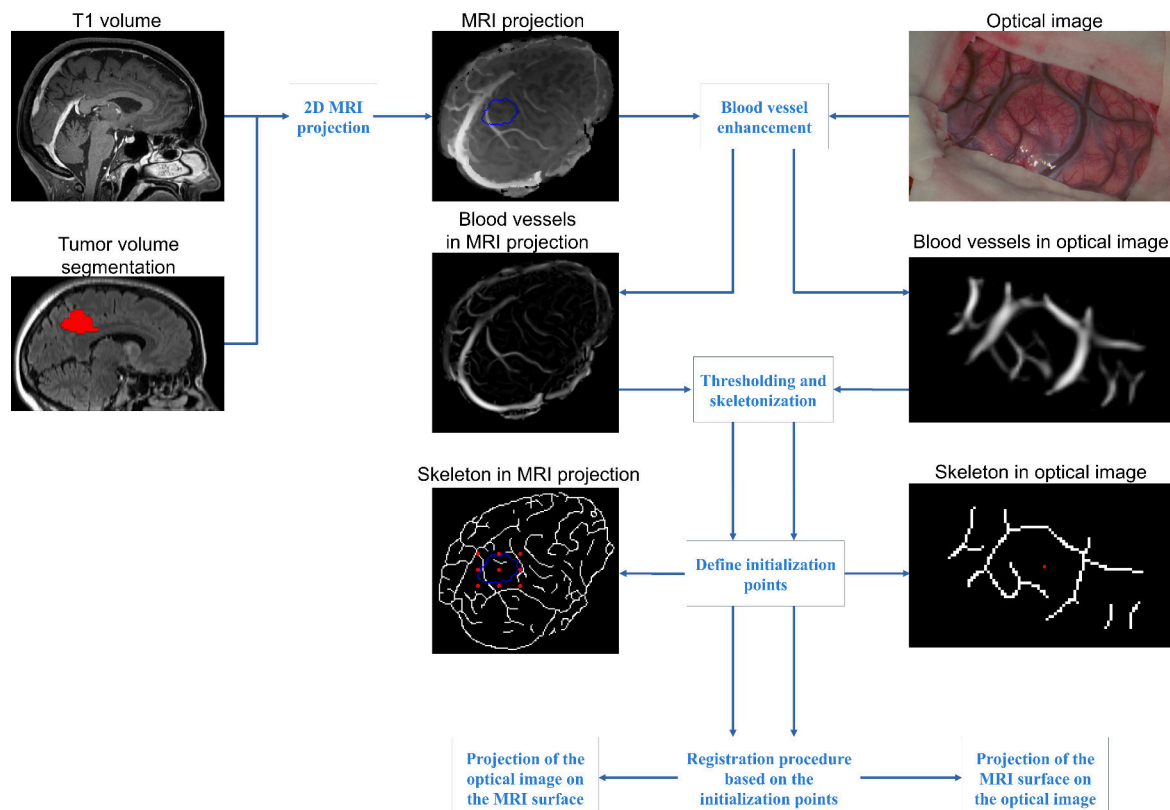


Figure 3: Flowchart of data analysis, including definitions of the imaging modalities and image processing techniques used in the automatic registration pipeline. In the T1 projection, the blue contours represented the delineation of the tumor. The red points in the optical and T1 images corresponded to points used to initialize the registration.

2.1 Projection of the T1 volume

In our study, the registration of a 2D optical image on a 3D MRI volume is a complex problem because these data have geometric differences. Indeed, the 2D optical image may have perspective distortions depending on the position of the camera relative to the patient brain. The compensation of these distortions requires a robust calibration of the camera relative to the patient brain (position, focal length, angle ...) that cannot be easily performed in the critical context of the surgical room.

To simplify the problem, we decided to register the 2D optical image on a 2D projection of the T1 volume. The steps performed to create the projection of the T1 volume are represented in Fig. 4 and are enumerated below:

1. The brain was extracted from the T1 volume using HD-Bet [11].
2. The binary mask of the tumor was registered on the T1 volume with a rigid transform using the framework itk-elastix in Python [15, 19].
3. The T1 volume was rotated so that the transverse axis of the MRI coincides with the axis passing through the origin of the MRI volume (one of the corners of the volume) and the center of gravity of the tumor. The center of rotation was the center of gravity of the MRI volume.
4. The 2D projection was obtained with an orthogonal projection along the transverse axis.

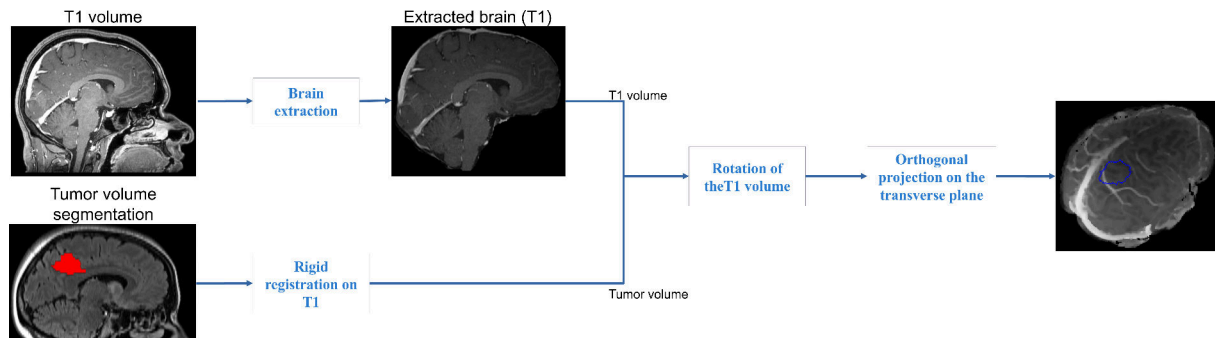


Figure 4: Steps executed to create the projection of the T1 volume. The blue contour represented the delineation of the tumor.

2.2 Segmentation of the blood vessels MR and optical images

The large blood vessels were segmented in the 2D projection of the T1 volume (see Fig. 4) and in the optical image (see Fig. 3) with a Hessian-based Frangi vesselness filter [7]. This filter was applied with the framework itk in Python [13, 24] at the image pixel level and is based on the eigenvalue decomposition of the local Hessian matrix of the image.

The Hessian-based Frangi vesselness filter accentuates the contrast between tubular objects (blood vessels) and the background. The filter also incorporates a multiscale smoothing, performed with several Gaussian filters having different standard deviation values. It is used to determine the probability of a voxel belonging to a vessel of a particular diameter.

For the 2D projection of the T1 volume and the optical image, we used five different scales from N mm to 3 mm to detect the large blood vessels. N corresponds to the resolution of the T1 volume, such that the filter is able to detect the smallest blood vessels in the MR image. The parameters were the same for the two images, the scale in pixels was adapted with the resolution of the images.

The Hessian-based Frangi vesselness filter has to be applied to grayscale images. For color optical imaging, the filter was used with the image of the red channel because, for the wavelengths captured by this channel, the absorption of light by the blood is lower than for the other channels. As a result, the contrast measured between grey matter and small blood vessels (< 1 mm) is lower for this channel than for the others. However, the contrast between large blood vessels (> 1 mm) and grey matter is still significant, see Fig. 5 B. In the case of a hyperspectral image, a wavelength or a combination of wavelengths in the near infrared can be used, see Fig. 5 C.

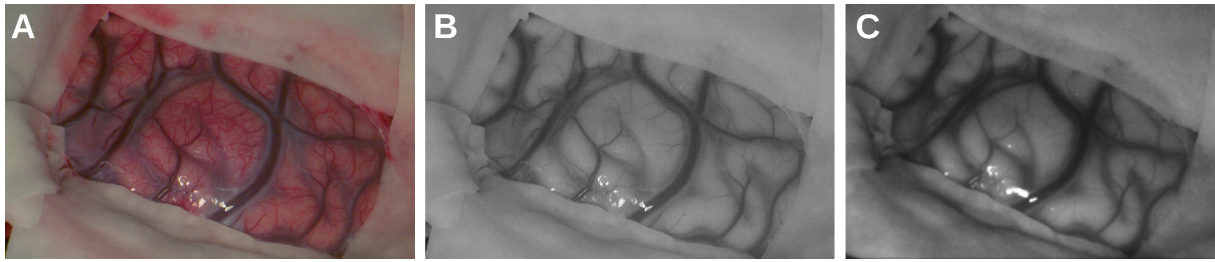


Figure 5: Optical images used by the Hessian-based Frangi vesselness filter for patient 1. A – Color image acquired with a commercial color camera (BASLER acA2000-165uc). B – Red channel of the color image A. C – Image acquired at 790 nm with a commercial hyperspectral camera (XIMEA MQ022HG-IM-SM5X5-NIR).

The images obtained after applying the Hessian-based Frangi vesselness filter on the MRI and optical images are represented in Fig. 6 B and Fig. 7 B. Then, these images were thresholded to get a binary image of the large blood vessels. We applied an arbitrary threshold of 15% of the maximum gray scale value for the optical image and a threshold of 4% of the maximum gray scale value for the MR image [1]. The binary optical image was undersampled to match the resolution of the MR image. Finally, the topology of the blood vessels was extracted with a skeletonization algorithm, see Fig. 6 C and Fig. 7 C.

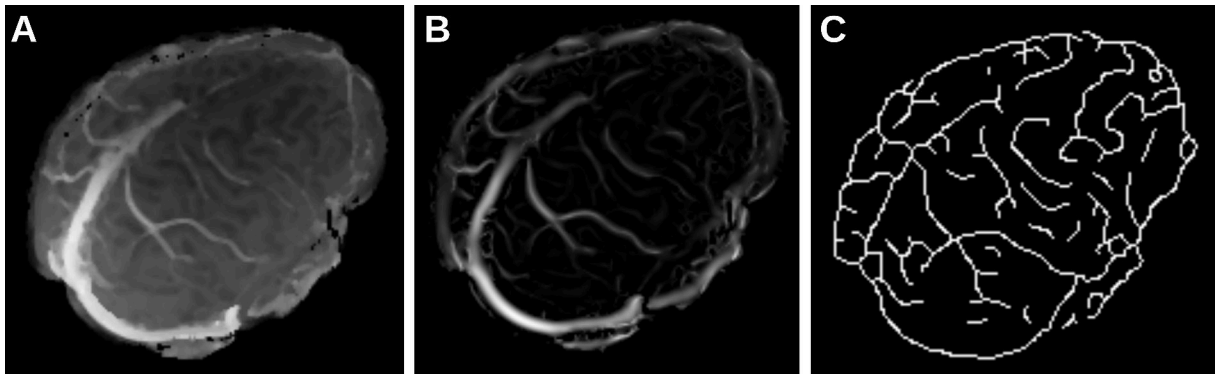


Figure 6: Segmentation of large blood vessel on the 2D projection of the T1 volume for patient 1. A - 2D projection of the T1 volume. B - Image with enhanced blood vessels. C - Image after thresholding and skeletonization.



Figure 7: Segmentation of large blood vessel on the optical image for patient 1. A - Red channel of the color image. B - Image with enhanced blood vessels. C - Image after thresholding and skeletonization.

2.3 Registration procedure

Using the skeletons of the blood vessels in the MR and optical images, we calculated the similarity transform that can be apply to the optical skeleton to match the MRI skeleton. A similarity transformation is defined as:

$$T(x) = sR(x - c) + t + c, \quad (1)$$

with s a scalar, R a rotation matrix, c the centre of rotation and t a translation vector. This means that the image is treated as an object, which can translate, rotate, and scale isotropically. The registration procedure was performed with the framework itk-elastic in Python [15, 19] with the following parameters:

Transform	Similarity transform
Optimizer	Quasi-Newton method
Metric	Normalized correlation
Fixed center of rotation	Initialization point
Multi resolution registration	No

Table 2: Parameters used with the framework itk-elastic.

The normalized correlation coefficient NCC was calculated between the fixed image I_F and the moving image I_M which had undergone the similarity transform T (see Eq. (1)):

$$NCC(I_F, I_M) = \frac{\sum_{x_i \in \Omega_F} ((I_F(x_i) - \overline{I_F}) (I_M(T(x_i)) - \overline{I_M}))}{\sqrt{\sum_{x_i \in \Omega_F} (I_F(x_i) - \overline{I_F})^2 \sum_{x_i \in \Omega_F} (I_M(T(x_i)) - \overline{I_M})^2}}, \quad (2)$$

with Ω_F the domain of the fixed image I_F and $\overline{I_F}$ and $\overline{I_M}$ the average grey-value of the images I_F and I_M , respectively. In Fig. 8, we represented an overview of the registration procedure.

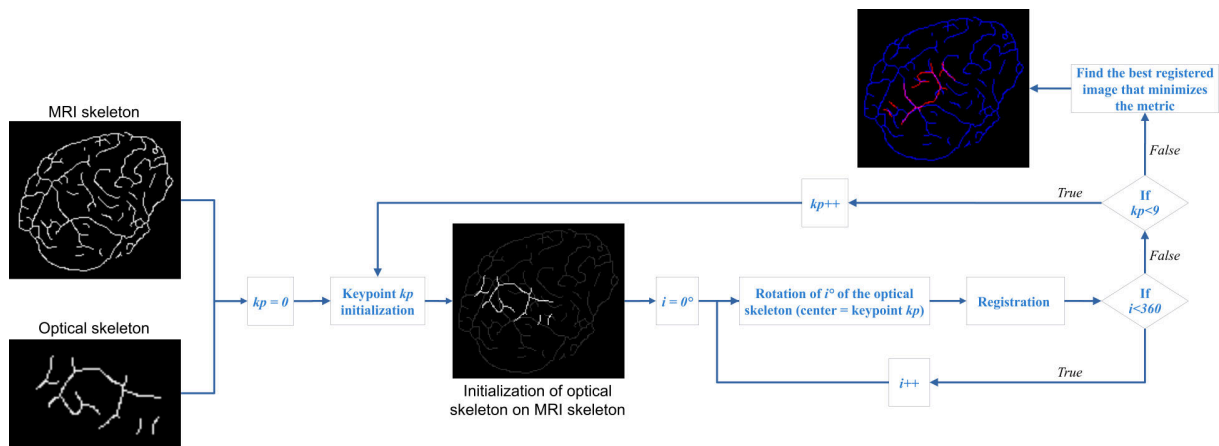


Figure 8: Registration procedure of the optical skeleton to the MRI skeleton. The procedure is composed on an iterative keypoint initialization, an iterative registration of the rotated optical skeleton and the selection of the best registered image.

The optical skeleton was registered with two interlocking iterative processes:

1. The optical skeleton was placed on the MRI skeleton using keypoints, see figure 8. The keypoint in the optical image (red point in figure 8 B) was iteratively placed on a keypoint of the MRI skeleton (red points in Fig. 9 A).

On the MRI skeleton, nine different keypoints located around the tumor were defined to help the convergence of the registration. The keypoints were located at the centre, the four vertices and the four centres of each side of the rectangle encompassing the contour of the tumour. In Fig. 9, the keypoints and the contour of the tumor are indicated in red and in blue, respectively.

On the optical skeleton, only one keypoint was defined and located at the center of mass of the surgical window. Indeed, as we indicated in table 1, the center of the tumor is usually close to the center of the surgical window. Thus, the keypoint in the optical image should be close to the center of the tumor.

If this criterion is not valid, the user can manually select a keypoint in the MR and the optical images. The optical and MRI keypoints can also be identified in the optical image and the MRI volume using the neuronavigation system during the neurosurgery.

2. Once the optical skeleton was placed on the MRI at the keypoint location, the optical skeleton was rotated and registered. The image was rotated with an angle included between 0° and 360° every 1° . These angles were tested to help the convergence of the registration and avoid a poor intersection between the two binary masks.

In Fig. 10, we represented the registration metric calculated during the two interlocking iterative processes as well as the optical skeleton registered on the MRI skeleton for the similarity transform that

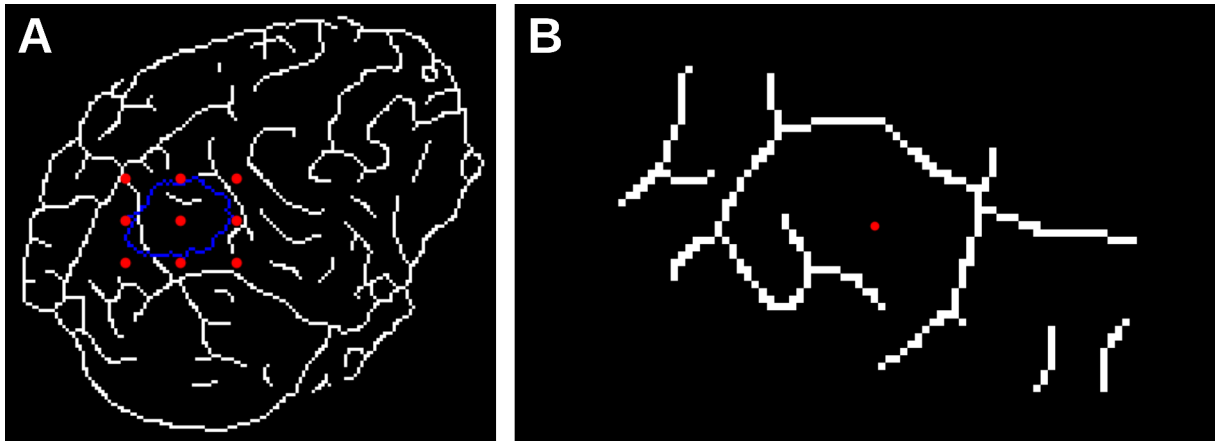


Figure 9: Keyoints in MRI (A) and optical (B) skeletons for patient 1. The blue contour indicated the delineation of the tumor.

minimized the metric. The nine colours used to plots the registration metrics in image A corresponded to the metrics calculated for the 9 keypoints. The whole registration process was performed in 7 min on a laptop (processor: 12th Gen Intel Core i7-12800H \times 20, RAM: 32 GB).

The minimum registration metric (normalized correlation = -0.19) was calculated for a rotation angle of 92° using the keypoint located at the center of the tumor. Low normalized correlation values are only obtained with this keypoint and for a rotation angle around 92° , which indicates the registration procedure is very dependent of the keypoint initialization and requires a complete rotation of the optical skeleton (all angles between 0° and 360°).

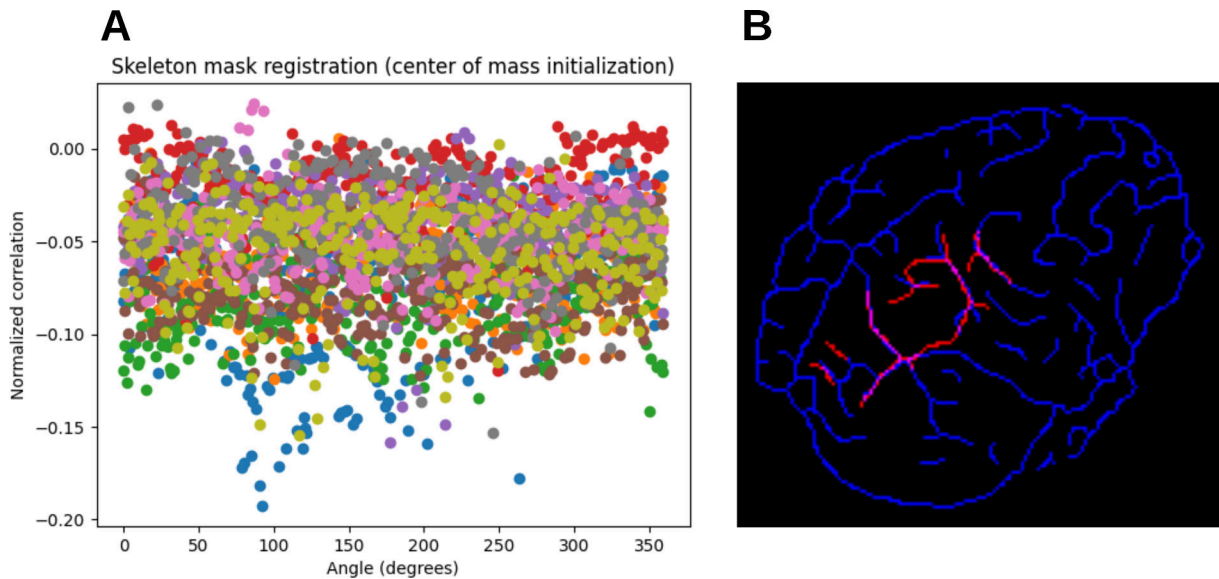


Figure 10: Registration results for patient 1. A - Registration metric calculated during the two interlocking iterative processes. B - Optical skeleton (in red) registered on the MRI skeleton (in blue) for the similarity transform that minimized the metric. The magenta pixels indicated an overlap between the optical and MRI skeletons.

2.4 Reconstruction of the optical image on the MRI volume

In section 2.3, we described the steps to calculate the similarity transform that can be applied to the optical skeleton to match the MRI skeleton. Once this transform has been calculated, it can be applied to other optical images for a projection on the MRI volume, see Fig. 11.

In this procedure, the optical image can be a color image (like Fig. 11) but can also be a statistical image that delineates a brain function in the optical image [4]. First, the optical image was undersampled to match the resolution of the MR image (see section 2.2). Then, the optical image was rotated. The

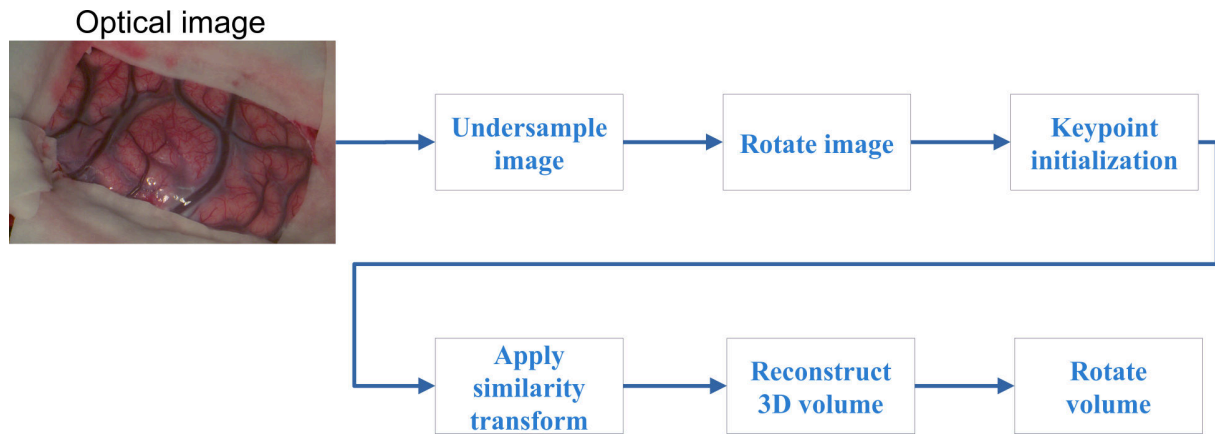


Figure 11: Procedure to project an optical image on the anatomical MRI volume (T1).

angle of rotation was identified during the registration procedure, see section 2.3. The rotated image was placed on the MRI projection with the keypoint identified in section 2.3. Then, the similarity transform was applied to the rotated image. The RGB registered on the MRI projection is represented in Fig. 12.

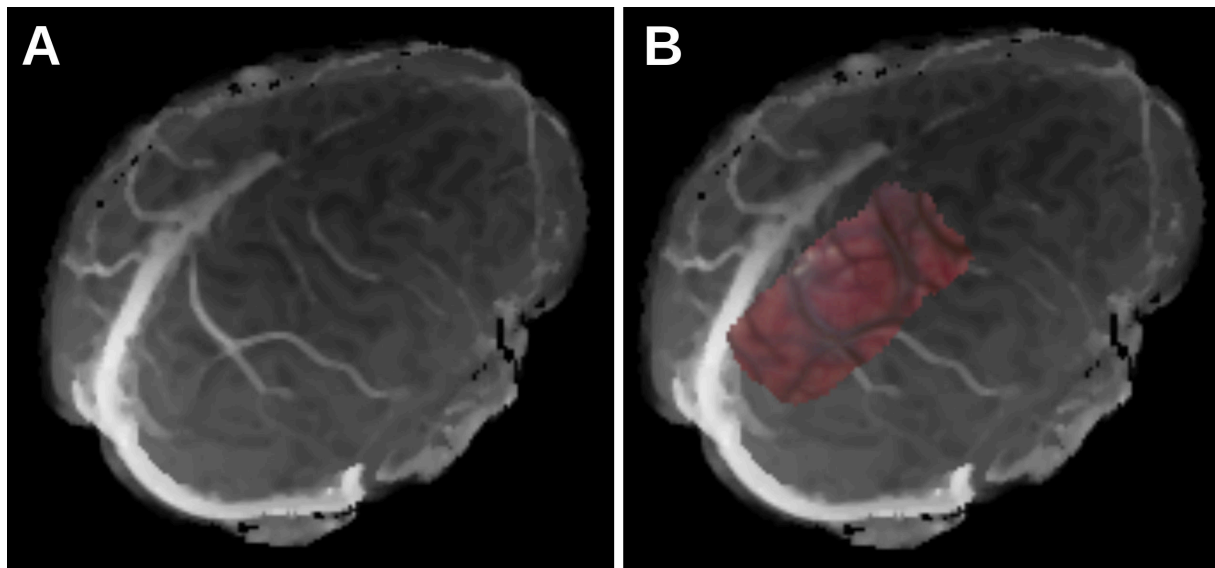


Figure 12: Registration of the optical image on the MRI projection for patient 1. A – MRI projection. B – Optical image registered on the MRI projection (A).

With the image registered on the MRI projection, a 3D volume of the optical image can be reconstructed. For each pixel (x,y) of the MRI projection having a non-null RGB value (see Fig. 12 B), the location of the surface of the MRI volume along the z axis was identified (first non-null values of the mask of the brain surface). The voxels found at these positions took on the value of the optical image. Finally, the reconstructed optical volume was rotated to get back to the space of the T1 volume (see section 2.1).

This reconstruction procedure was applied to the optical statistical image used to identify the motor cortex, see Fig. 13. Details regarding the calculation of this statistical map can be found in Ref [4]. The T1 volume is represented with three overlays. In red, we represented the pre-operative fMRI map (binary mask) obtained with a left finger tapping task. In blue, we represented the intraoperative functional optics map (binary mask) obtained with a finger tapping task. The white contour represents the contour of the surgical window (see image in figure 12 A). We can observe a good correlation between the functional identifications provided by fMRI and optical imaging, see section 2.5 for more details.

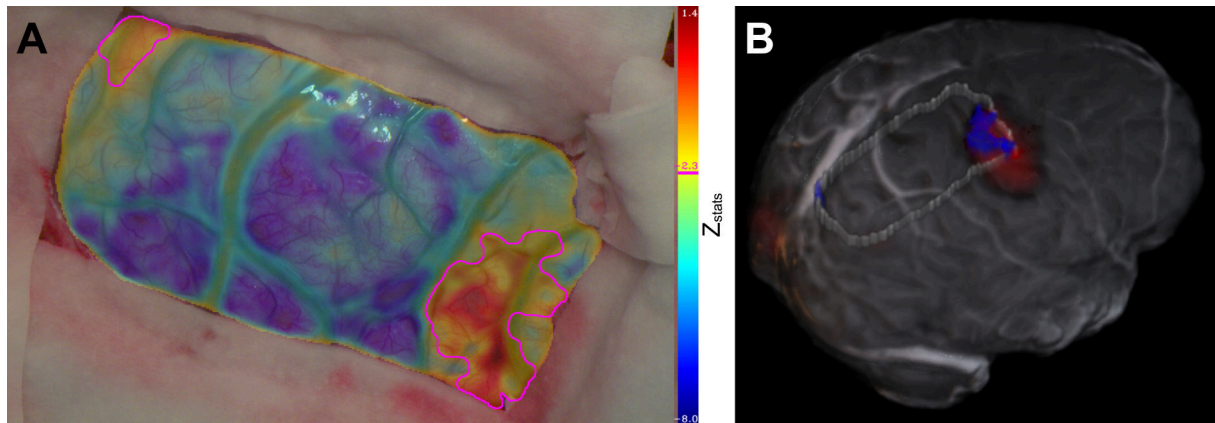


Figure 13: Reconstruction procedure applied to intraoperative functional brain map obtained with RGB imaging for patient 1. A - Intraoperative functional brain map obtained with RGB imaging [3]. The magenta contour is represented by the volume in blue on image B. B - T1 MRI volume and three overlays. The preoperative fMRI (left finger tapping) is represented in red, the intraoperative functional optics is represented in blue (left finger tapping). The surgical window is represented with a white contour.

2.5 Projection of the MRI volume on the optical window

In section 2.3, we described the steps to calculate the similarity transform that can be applied to the optical skeleton to match the MRI skeleton. Once this transform has been calculated, its inverse transform can be estimated to reconstruct the MRI volume in the optical space, see Fig. 14.

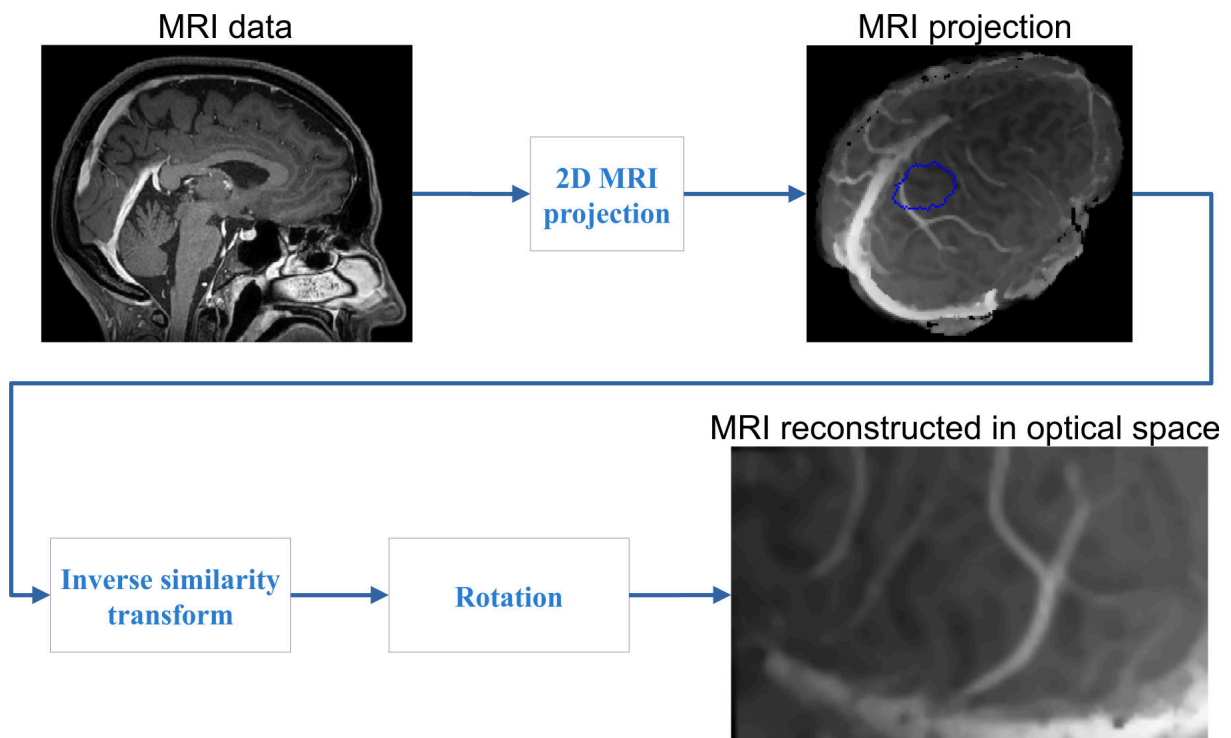


Figure 14: Procedure to reconstruct MRI data in the optical space.

First, a 2D projection of the MRI volume was calculated, see details in section 2.1. Using the inverse similarity transform, the MRI projection was reconstructed in the space of the rotated optical image that was used to calculate the similarity transform, see section 2.3. Finally, the reconstructed MRI image was rotated to match the orientation of the initial image.

In Fig. 15, we represented the reconstruction of the T1 volume in the optical space. In image A, the reconstructed image is represented in false color. In image B, the reference optical image is plotted. In both images, the green contour represented the contour of the surgical window and the gray overlay represented the blood vessel skeleton calculated with the optical image B, see section 2.2. The validation

of the registration method has been evaluated in section 3.

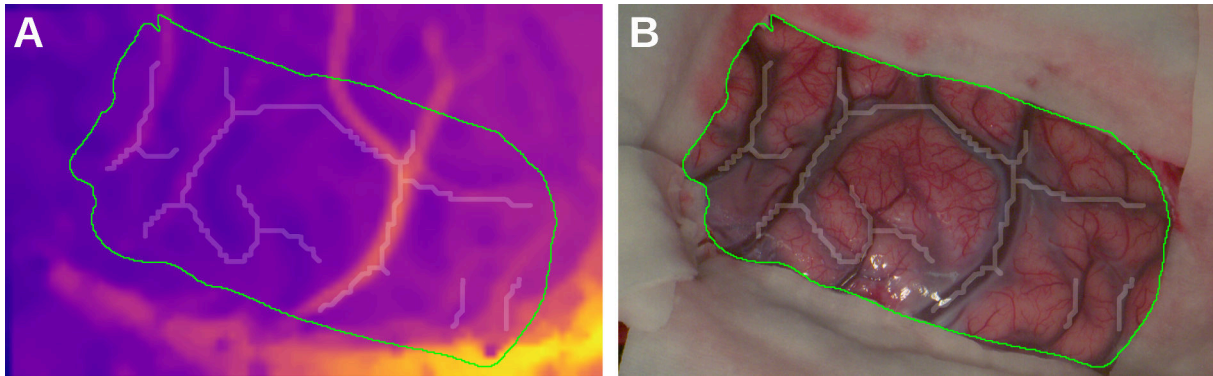


Figure 15: Reconstruction of the T1 MRI volume in the optical space for patient 1. A – MRI reconstructed image. B – Reference optical image. In both images, the green contour represented the contour of the surgical window and the gray overlay represented the blood vessel skeleton calculated with the optical image B.

This reconstruction procedure was applied to the fMRI statistical image used to identify the motor cortex. In Fig. 16, we represented the optical image with two contours obtained from the statistical maps (contours of the statistical inferences). The red and blue contours indicated the delineation of the motor cortex identified with fMRI and optical imaging, respectively.

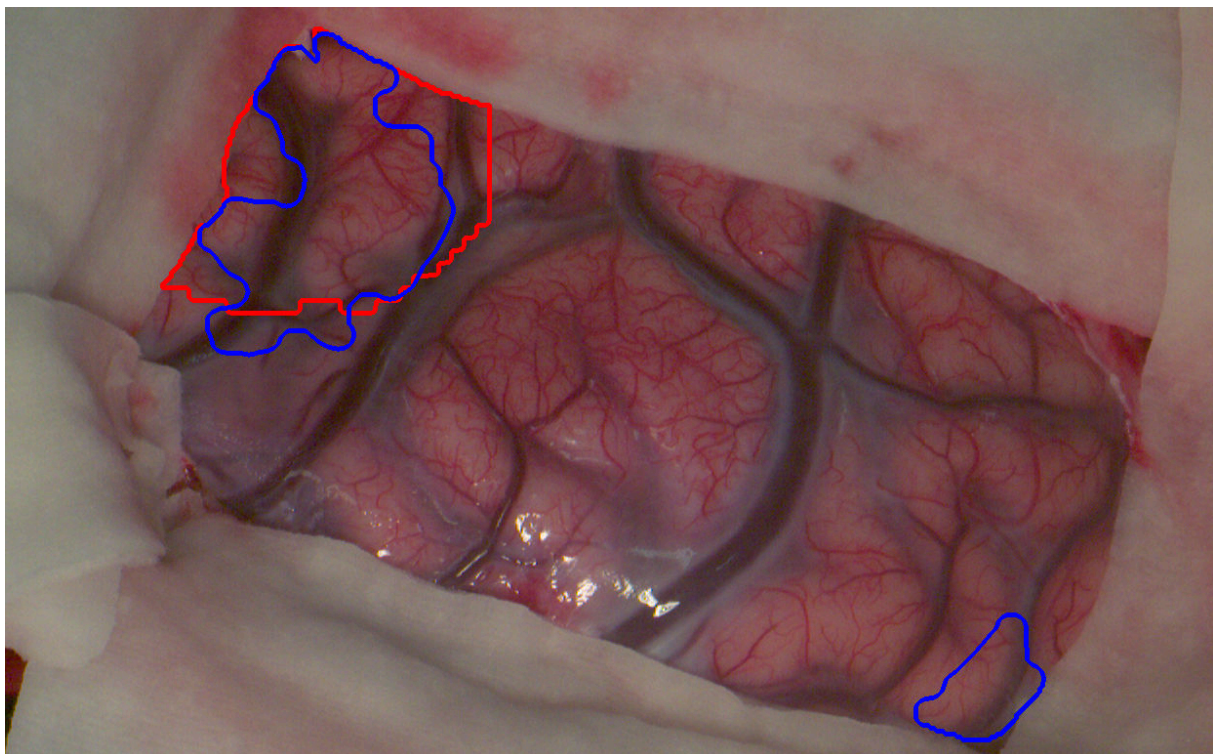


Figure 16: Contours of the functional statistical maps represented on the optical image for patient 1. The red and blue contours indicated the delineation of the motor cortex identified with fMRI and optical imaging, respectively.

The DICE coefficient [6] was computed between the binary functional masks obtained with fMRI and optical imaging, see Fig. 16. The DICE coefficient was 0.71, which indicates a good correspondence between the two binary masks. However, we can observe some differences between the functional statistical maps. On the top left image, the area of the optical functional mask (blue contour) is smaller than that of the fMRI mask (red contour). On the bottom right image, a portion of the gray matter is identified as activated with optical imaging, but not with fMRI. This could be explained by the differences of the contrasts measured by optical imaging and fMRI. fMRI is related to the measure of the BOLD signal (Blood Oxygen Level Dependent) which reflects the changes in the paramagnetic properties of

deoxygenated hemoglobin following the neuronal activation. The fluctuation of the BOLD signal varies with the cerebral blood flow and volume with a poor spatial resolution (≈ 1 mm) compared to that of optical imaging (≈ 70 μm). On the contrary, optical imaging relies on a direct measurement of oxy- and deoxygenated hemoglobin due to the blood volume changes that follows the neuronal activity. These differences in the spatial resolution and in the origin of the contrast may explain the differences between the functional identifications. This hypothesis was also expressed in a study conducted by Narayan et al. [14]. The authors indicated that the differences observed between fMRI and optical imaging may be due to the venous origin of the BOLD fMRI signal, when some studies point that the origin of the optical signal is more arterial. These hypothesis are currently investigated in WP5 to improve the correlation of intraoperative optical biomarkers and clinical fMRI biomarkers.

3 Validation of the registration algorithm

The registration algorithm has been verified with 9 patients using a landmark-based validation approach [5]. With this method, the accuracy of alignment between two images is evaluated by comparing anatomical or structural points (landmarks) in both images. At least three landmarks were manually selected based on distinct identifiable features in both images such as the intersection of two blood vessels. After the registration process, the mean and standard deviation of the Euclidean distance (in mm) were calculated between the corresponding landmarks, giving a quantitative metric for the evaluation of the registration process.

In Fig. 17, we represented the landmarks used to validate the registration method. The registered landmarks are represented with red stars in the registered image (A) and in the fixed image (MRI projection, image B). The landmarks selected in the MRI projected are represented with green points in image B.

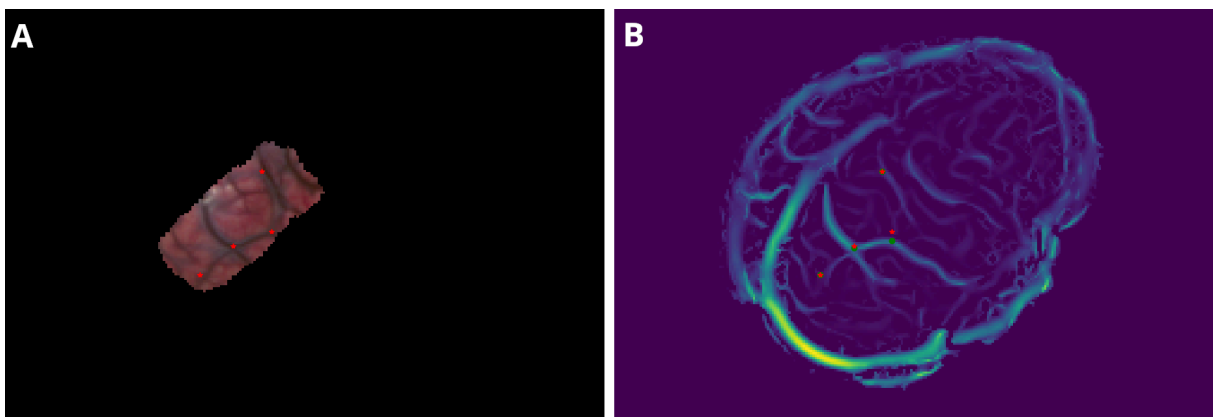


Figure 17: Landmarks used to validate the registration method for patient 1. A – Registered optical images and landmarks (red stars). B – Registered landmarks (red stars) and landmarks of the fixed image (green points).

In table 3, we indicated the mean and standard deviation of the Euclidean distance calculated for the 9 patients of this study.

Patient ID	Registration type	MRI projection resolution (mm)	Euclidean distance (mm) (mean \pm standard deviation)
1	Automatic	1	1,32 \pm 1,27
2	Automatic	0,46	1,30 \pm 0,22
3	Automatic	0,46	1,08 \pm 0,15
4	Manual selection of the keypoints	0,46	2,38 \pm 1,72
5	Manual selection of the keypoints	0,46	1,77 \pm 0,48
6	Automatic	0,90	1,22 \pm 1,00
7	Automatic	0,46	1,06 \pm 0,46
8	Automatic	0,46	1,65 \pm 0,56
9	Automatic	0,5	1,09 \pm 0,67

Table 3: Mean and standard deviation of the Euclidean distance calculated for the 9 patients in this study.

The automatic registration procedure was performed with the 9 patients of our study, see Fig. 18 in the appendix. The registration was successfully executed for 7 patients. For 2 patients (patients 4 and 5), the automatic registration procedure was put into default. The registration was achieved with the manual selection of the MRI and optical keypoints, see section 2.3. Indeed, the automatic procedure, based on the use of keypoints located around the tumor, did not lead to convergence of the registration process. For these two patients, this failure can be explained by the fact that the conditions set out in table 1 were not met. The optical image was obtained with a surgical microscope that did not acquire the whole surgical window. Moreover, the image was centered on the functional area and not on the tumor. Thus, the optical keypoint was not located near the MRI keypoints, which put the automatic registration procedure into default. To overcome this failure, we manually selected a pair of optical/MRI keypoints.

With the landmark-based validation approach, the average Euclidean distance between the optical and MRI validation landmarks is $1,43 \pm 0,72$ mm, which corresponds to an errors of $2,77 \pm 1,2$ pixels. This results are very promising, indeed, the mean registration error is less than the mean error obtained by Villa et al (1.88 ± 0.19 mm) [22]. Although Villa et al obtained smaller standard deviation error, our method has the advantage to be directly used in the clinical routine, whereas the method proposed by Villa et al requires the use of a dedicated imaging system composed of 2 cameras (including a RGB-Depth camera providing geometric data through a depth-sensing device) and a tracking system.

4 Areas for improvement

- The automatic registration pipeline uses the tumor volume segmentation for the calculation of a 2D projection of the T1 volume, see section 2.1. In Lyon and Saint-Etienne hospitals, the segmentation of the tumor is a part of the clinical standard, but it is not the case for all hospitals, see table 1. To overcome this limitation, an automatic segmentation of the tumor volume can be implemented. For this purpose, the BraTS toolkit [12] can be used.
- The robustness of the registration procedure can be improved, see section 2.3. The procedure relies on the identification of the best similarity transform that minimizes the registration metric (normalized correlation coefficient, see Eq. (2)). In Fig. 10, we can see that the minimum metric is found for a rotation angle of 92° of the optical image. Although the registration procedure converges, the robustness of the registration procedure could be improved by decreasing the value of the metric. This could be achieved by combining multiple registration metrics and multiple fixed and moving images. In addition to the actual registration procedure, signed distance images could be registered with a mean square difference metric. The signed distance images are obtained with a distance transform of binary skeleton masks (distance from every binary image pixel to the nearest zero pixel).
- In order to improve the precision of the registration process, a 3D non-rigid transform (b-spline) can be added to the registration procedure. This transform can be used after the reconstruction of the optical volume to have to better match of the cerebral structures.
- Some parameters of the procedure (scales of the Hessian-based Frangi vesselness filter, segmentation thresholds) have to be adapted depending on the image, see section 2.2. For some patients, the registration procedure used large blood vessels (≈ 3 mm) to match the common structures in the optical and MR images. However, for other patients, the registration procedure used small and large blood vessels, which requires the detection of vessels width at the MRI resolution. In order to solve this problem, an automatic segmentation of the blood vessels in MR and optical images can be implemented using deep learning. For this purpose, we are working with our collaborators of Technical University of Munchen.
- The automatic keypoints position around the tumor can be improved. Indeed, we saw that the method was put into default for 2 patients, see table 3. An automatic search of optical and MRI keypoints can be initialized using feature matching [20].

The definition of the optical and MRI keypoints could also be improved with the acquisition of optical images with a field of view centered on the entire surgical window (see table 1). An other approach could be to propose a second longer registration pipeline, in case the first one fails, using more and more distant starting point to cover a broader area around the tumor location.

- We plan to investigate a new approach to register optical images on preoperative or postoperative MRI T1 volumes.

The BraTS toolkit contains a huge dataset of T1 volumes. For each volume, several 2D projections could be created from the extracted T1 volumes. From these projections, we can create synthetic optical images with the addition of supplementary blood vessels of various diameters. Using this dataset, we can train a neural network (UNET) to calculate the similarity transform for projecting the synthetic optical image on the MRI volume. For this future work, we plan to work with our collaborators of Technical University of Munchen.

Appendix

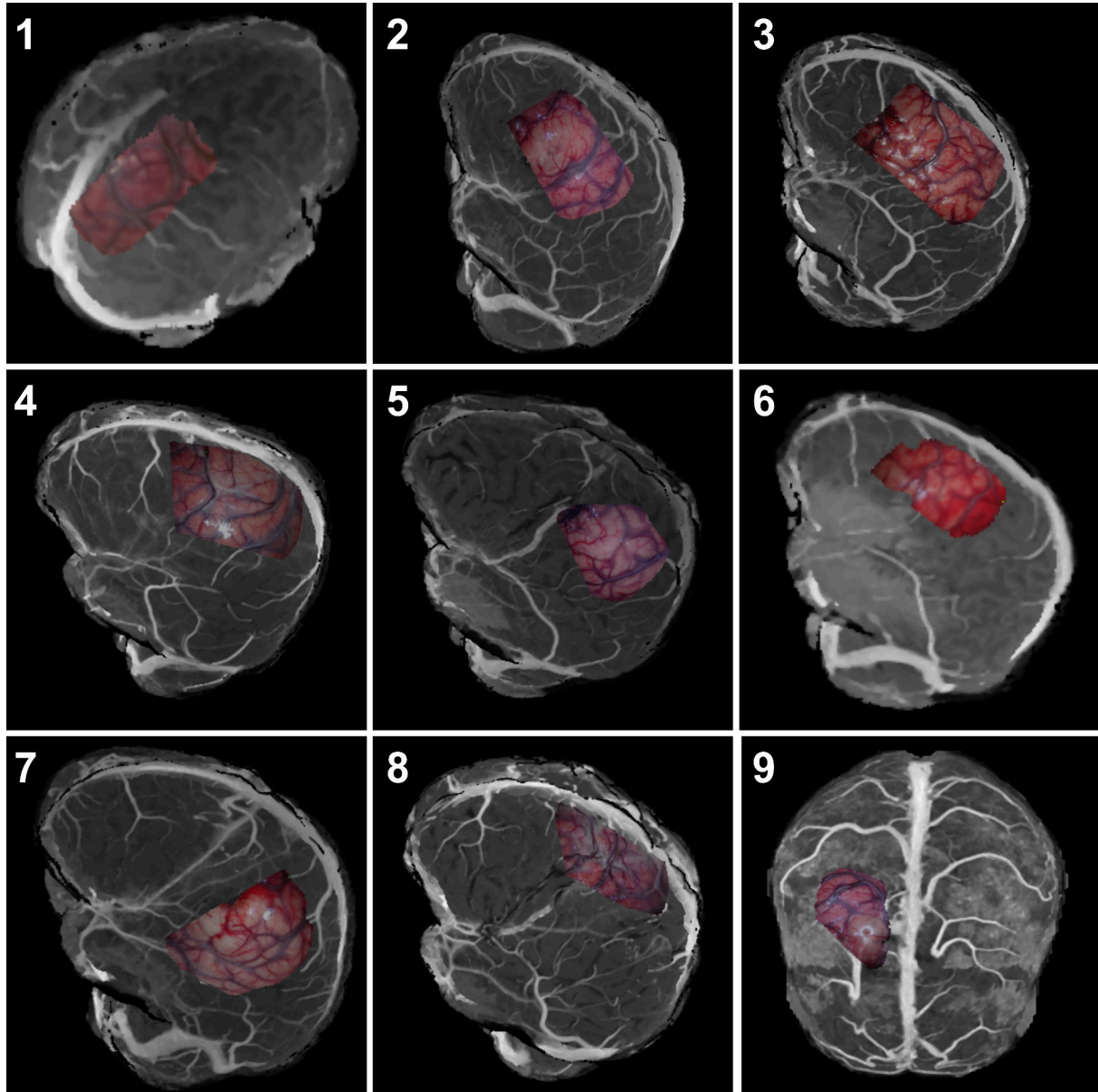


Figure 18: Optics to MRI registration results obtained for patient 1 to 9.

References

- [1] S. Avadiappan, S. Payabvash, M. A. Morrison, A. Jakary, C. P. Hess, and J. M. Lupo. A fully automated method for segmenting arteries and quantifying vessel radii on magnetic resonance angiography images of varying projection thickness. *Frontiers in Neuroscience*, 14:537, 2020.
- [2] G. Bradski. The opencv library. *Dr. Dobb's Journal: Software Tools for the Professional Programmer*, 25(11):120–123, 2000.
- [3] A. F. Cannestra, N. Pouratian, S. Y. Bookheimer, N. A. Martin, D. P. Becker, and A. W. Toga. Temporal spatial differences observed by functional MRI and human intraoperative optical imaging. 11(8):773–782.
- [4] C. Caredda, E. Van Reeth, L. Mahieu-Williams, R. Sablong, M. Sdika, F. C. Schneider, T. Picart, J. Guyotat, and B. Montcel. Intraoperative identification of functional brain areas with rgb imaging using statistical parametric mapping: Simulation and clinical studies. *NeuroImage*, 278:120286, 2023.
- [5] R. Castillo, E. Castillo, R. Guerra, V. E. Johnson, T. McPhail, A. K. Garg, and T. Guerrero. A framework for evaluation of deformable image registration spatial accuracy using large landmark point sets. *Physics in Medicine & Biology*, 54(7):1849, 2009.
- [6] L. R. Dice. Measures of the amount of ecologic association between species. *Ecology*, 26(3):297–302, 1945.
- [7] A. F. Frangi, W. J. Niessen, K. L. Vincken, and M. A. Viergever. Multiscale vessel enhancement filtering. In *Medical Image Computing and Computer-Assisted Intervention—MICCAI'98: First International Conference Cambridge, MA, USA, October 11–13, 1998 Proceedings 1*, pages 130–137. Springer, 1998.
- [8] T. Gasser, O. Ganslandt, E. Sandalcioğlu, D. Stolke, R. Fahlbusch, and C. Nimsky. Intraoperative functional MRI: Implementation and preliminary experience. *NeuroImage*, 26(3):685–693, July 2005.
- [9] A. Gautheron, J. Bernstock, T. Picart, J. Guyotat, P. Valdés, and B. Montcel. 5-ala induced ppix fluorescence spectroscopy in neurosurgery: a review. *Frontiers in Neuroscience*, 18:1310282, 2024.
- [10] I. J. Gerard, M. Kersten-Oertel, K. Petrecca, D. Sirhan, J. A. Hall, and D. L. Collins. Brain shift in neuronavigation of brain tumors: A review. *Medical Image Analysis*, 35:403–420, 1 2017.
- [11] F. Isensee, M. Schell, I. Pflueger, G. Brugnara, D. Bonekamp, U. Neuberger, A. Wick, H.-P. Schlemmer, S. Heiland, W. Wick, et al. Automated brain extraction of multisequence mri using artificial neural networks. *Human brain mapping*, 40(17):4952–4964, 2019.
- [12] F. Kofler, C. Berger, D. Waldmannstetter, J. Lipkova, I. Ezhov, G. Tetteh, J. Kirschke, C. Zimmer, B. Wiestler, and B. H. Menze. Brats toolkit: translating brats brain tumor segmentation algorithms into clinical and scientific practice. *Frontiers in neuroscience*, 14:125, 2020.
- [13] M. M. McCormick, X. Liu, L. Ibanez, J. Jomier, and C. Marion. ITK: enabling reproducible research and open science. 8. Publisher: Frontiers.
- [14] S. M. Narayan, P. Esfahani, A. J. Blood, L. Sikkens, and A. W. Toga. Functional increases in cerebral blood volume over somatosensory cortex. *Journal of Cerebral Blood Flow & Metabolism*, 15(5):754–765, 1995.
- [15] K. Ntatsis, N. Dekker, V. v. d. Valk, T. Birdsong, D. Zukić, S. Klein, M. Staring, and M. McCormick. itk-elastic: Medical image registration in python. In M. Agarwal, C. Calloway, and D. Niederhut, editors, *Proceedings of the 22nd Python in Science Conference*, pages 101 – 105.
- [16] M. Oelschlägel, T. Meyer, U. Morgenstern, H. Wahl, J. Gerber, G. Reiß, E. Koch, G. Steiner, M. Kirsch, G. Schackert, and S. B. Sobottka. Mapping of language and motor function during awake neurosurgery with intraoperative optical imaging. 48(2):E3.
- [17] J. Pallud, E. Mandonnet, R. Corns, E. Dezamis, E. Parraga, M. Zanello, and G. Spina. Technical principles of direct bipolar electrostimulation for cortical and subcortical mapping in awake craniotomy. *Neurochirurgie*, 63(3):158–163, 6 2017.
- [18] T. Picart, A. Gautheron, C. Caredda, C. Ray, L. Mahieu-Williams, B. Montcel, and J. Guyotat. Fluorescence-guided surgical techniques in adult diffuse low-grade gliomas: State-of-the-art and emerging techniques: A systematic review. *Cancers*, 16(15), 2024.

- [19] D. P. Shamonin, E. E. Bron, B. P. Lelieveldt, M. Smits, S. Klein, and M. Staring. Fast parallel image registration on CPU and GPU for diagnostic classification of alzheimer’s disease. 7. Publisher: Frontiers.
- [20] S. Taylor, E. Rosten, and T. Drummond. Robust feature matching in 2.3 μ s. In *2009 IEEE Computer Society Conference on Computer Vision and Pattern Recognition Workshops*, pages 15–22. IEEE, 2009.
- [21] S. Van der Walt, J. L. Schönberger, J. Nunez-Iglesias, F. Boulogne, J. D. Warner, N. Yager, E. Gouillart, and T. Yu. scikit-image: image processing in python. *PeerJ*, 2:e453, 2014.
- [22] M. Villa, J. Sancho, G. Rosa, M. Chavarrias, E. Juarez, and C. Sanz. HyperMRI: hyperspectral and magnetic resonance fusion methodology for neurosurgery applications.
- [23] P. Virtanen, R. Gommers, T. E. Oliphant, M. Haberland, T. Reddy, D. Cournapeau, E. Burovski, P. Peterson, W. Weckesser, J. Bright, et al. Scipy 1.0: fundamental algorithms for scientific computing in python. *Nature methods*, 17(3):261–272, 2020.
- [24] T. S. Yoo, M. J. Ackerman, W. E. Lorensen, W. Schroeder, V. Chalana, S. Aylward, D. Metaxas, and R. Whitaker. Engineering and algorithm design for an image processing API: A technical report on ITK - the insight toolkit. In *Medicine Meets Virtual Reality 02/10*, pages 586–592. IOS Press.